Adaptive Virtual Capacitor Control for MTDC System With Deloaded Wind Power Plants

CHENG ZHONG, (Member, IEEE), **JIALONG ZHANG**, (Graduate Student Member, IEEE), **AND YANG ZHOU**, (Graduate Student Member, IEEE)

Key Laboratory of Modern Power System Simulation and Control and Renewable Energy Technology (Ministry of Education), Northeast Electric Power University, Jilin 132012, China

Corresponding author: Cheng Zhong (zhongcheng@neepu.edu.cn)

ABSTRACT Coordinated droop control strategies can provide frequency support for AC area grids from wind farms integrated through multi-terminal high-voltage DC (MTDC) transmission. However, such a strategy inevitably causes DC voltage deviation for transmitting AC area frequency information, thereby deteriorating the stability and security of the MTDC system operation. This paper reports an improved adaptive virtual capacitor control strategy that can provide inertial support for the system. Instead of increasing the capacitance of the physical capacitor, a virtual capacitor is generated by utilizing the rest energy of the deloaded wind farm. Furthermore, an S-shape function is designed to adaptively adjust the capacitance of the virtual capacitor based on the operating points of the system, in order to provide a better inertial support than with the fixed virtual capacitor control strategy. The proposed strategy not only enhances the DC voltage nadir but also improves the frequency nadir of the AC area by releasing additional power from the deloaded wind farm., a MTDC system of a four-terminal voltage source converter with two wind farms is simulated using PSCAD/EMTDC. Case studies are conducted to compare and demonstrate the effectiveness of the proposed strategy under sudden load variations.

INDEX TERMS Droop control, frequency regulation, wind farm, inertia response, virtual capacitor, VSC-MTDC.

I. INTRODUCTION

Wind power is gradually replacing fossil-fuel-based power, with the installed wind capacity increasing on a yearly basis. In 2019, a wind energy capacity of 60.4 GW was installed globally, which represents a 19% increase over 2018 and the second-highest yearly installation of wind energy historically. And the global wind energy capacity was more than 651 GW, which represents an increase of 10% compared to 2018 [1]. As voltage source converters (VSCs)-based (or modular multilevel converters) high-voltage DC (MTDC) transmission is economical and flexible, they are used for large-scale wind farm integration and energy transmission. Furthermore, multi-terminal high-voltage DC (MTDC) transmission is a suitable method for interconnecting multi-asynchronous power grids and wind farms [2], [3], and a four-terminal

The associate editor coordinating the review of this manuscript and approving it for publication was Kan Liu.

±500 kV high-voltage DC (HVDC) system is under development to interconnect large-scale onshore wind farms in the Zhangbei area [4].

However, wind farms are connected through VSC-based stations, which have to be decoupled from the AC grid system. The active power from MTDC systems can replace the power from conventional synchronous generators in the AC areas, can reduce the inertia of the system, and increase the risk of operation and frequency control ability in the AC areas.

Owing to their fast power regulation and flexible operation capability, VSC-MTDC systems can provide inertia and frequency regulation if the converters, such as wind turbines and VSC stations are designed appropriately. Two common control strategies for the VSC-MTDC system are the master-salver and DC-voltage droop control strategies.

In the master-salver strategy, only the master VSC station regulates the DC-bus voltage, whereas the other VSC stations

are operated in power injection control mode. A few frequency support strategies based on master-salver assignment have been proposed in [5], [6]. However, the master-salver assignment has the drawback that the DC-bus voltage stability completely relies on the master VSC station and requires fast communication between the master and salver stations.

In the DC-voltage droop control strategy, which is a distributed control strategy, all the grid-side stations participate in the DC-bus voltage regulation. Therefore, it is important to coordinate the power sharing between the multiple stations reliably and safely. However, the conventional droop control strategy determines the power sharing only between the grid-side stations and cannot provide frequency support for the AC areas. Many improved coordinated droop control strategies have been proposed to address this issue. In [7]–[9], the energy stored in the DC-link capacitor was utilized to provide inertia and frequency support. However, the stored energy was too little for the normal DC-link capacitor, so a larger capacitor had to be installed to obtain sufficient power and ensure that the voltage deviation was within the allowable range, increasing the investment cost and converter size.

There are two methods for provisioning the frequency response in wind farms: (i) inertia response from the rotor kinetic energy; and (ii) primary droop response from the deloaded wind farms. However, owing to the presence of the DC grid, the frequency of the main AC area is decoupled from the wind farms, which, thus, cannot directly sense the frequency deviation information of the main AC areas. Therefore, it is necessary to design an appropriate coordination control between the grid-side and wind-farm side stations. In [10]–[12], an auxiliary frequency control loop was proposed for the grid side stations. In this method, an auxiliary DC voltage droop controller converts the grid frequency signal into an DC-voltage deviation signal, and the DC-voltage deviation is converted to a wind farm side frequency-deviation signal through DC voltage and AC frequency droop ($V_{dc} - f$ droop) control. Thus, the wind farm releases the rotor kinetic energy for provisioning the inertia response similar to when they are directly connected to the AC areas. However, the rotor kinetic energy is limited and can only provide short-term frequency support. Owing to the long-term frequency drop in the AC power grid, this control strategy cannot provide long-term power support. In deloaded wind farms, the $V_{dc} - f$ droop control can provide long-term frequency response at the cost of wasting a portion of the captured wind energy [13]–[15]. In [16], deloaded wind turbine control was applied to an MTDC system, and the frequency change information on the grid side was transmitted as DC-voltage deviation information. When the frequency fluctuates in AC areas, the wind farm provides primary frequency support by releasing the pre-reserve energy of the deloaded wind farm. In [17], a mix control strategy was proposed to provide inertia support by utilizing the energy from HVDC capacitors and the kinetic energy of the wind turbines' rotors.

Frequency support can be provided by sharing power among AC areas. In [18]–[21], distributed PI controllers were proposed for both frequency regulation and power sharing among AC areas, requiring only local and neighboring state information. In [21], an improved pilot voltage droop-based control for MTDC systems was proposed and the desired frequency deviation among the AC connection areas after modifying the power reference of the droop-controlled VSCs was achieved. However, such methods require a real-time remote communication link between the grid-side stations; any communication delay or failure will affect the frequency regulation stability and security. Therefore, several coordination droop control strategies that do not require communication have been investigated for MTDC systems. In [22], an adaptive droop control strategy was proposed; in this strategy, the V-I-F characteristics were derived to establish a relationship between the frequency deviation and the DC voltage. The VSC station investigated in [22] could adaptively provide a DC voltage reference based on the grid frequency deviation and distribute the power of each converter station. Furthermore, in [23], [24], a V-P-F droop coordinate control was established for grid-side stations. However, these methods focused on the coordination control of the grid-side stations, without considering the frequency regulation ability of the wind farms.

In this study, we propose an adaptive virtual capacitor (AVC) control method for wind farm-side stations to provide suitable frequency responses and improve the DC-voltage drop during the frequency regulation period. Nevertheless, the coordination droop control method in [23], [24] was still used for the grid-side stations. The main contributions of this study are as follows:

(1) The rest energy of the deloaded wind farm is utilized to realize a virtual capacitor, which participates in the AC area frequency regulation and provides inertia support for the DC voltage; it is not necessary to install a dc capacitor with larger capacitance

(2) An S-shape function is designed to realize an adaptive droop control. The value of virtual capacitor is adjusted adaptively based on the MTDC system operating state.

A detailed four-terminal VSC-based MTDC system with two wind farms is built using PSCAD/EMTDC. The proposed AVC control strategy is tested in different load change cases. The simulation results show that the proposed method can effectively enhance the voltage nadir of the DC bus and the frequency nadir of the AC areas.

The rest of this paper is organized as follows. The four-terminal MTDC system with two wind farms and the conventional control strategy are discussed in Section II. Section III presents the AVC control for the wind farm-side stations. The simulation results are reported and discussed in Section IV. Finally, the conclusions are presented in Section V.

II. MULTI-TERMINAL HVDC WITH WIND FARMs
An MTDC system can have several different topologies. In this study, we used the four-terminal ring-net topology,
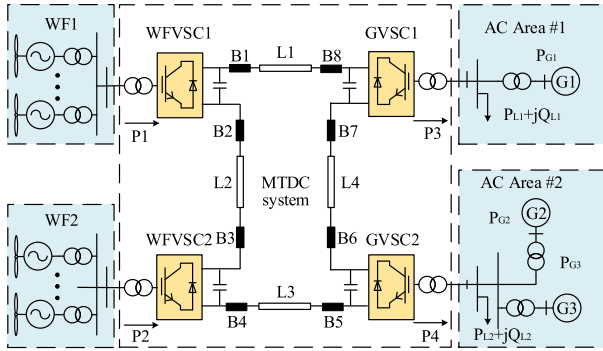
FIGURE 1. Schematic of a four-terminal HVDC system.

including two wind farm terminals and two AC area terminals, as shown in Fig. 1. This topology is derived from the Zhangbei ±500 kV four-terminal HVDC power grid demonstration project (China) [3].

Two wind farms, denoted as WF1 and WF2, were connected through two different wind farm-side VSCs (WFVSCs), denoted as WFVSC1 and WFVSC2, respectively. The capacities of WF1 and WF2 were 320 and 640 MVA, respectively. An aggregated model of wind turbines within the wind farms was used. Two independent AC asynchronous systems, denoted as AC area #1 and AC area #2, were connected through different grid-side VSCs (GVSCs), denoted as GVSC1 and GVSC2, respectively. B1~B8 are DC circuit breakers, which might include significant series inductors [25], [26].

The AC grid comprised synchronous generators and local loads. In AC area #1, the capacity of the synchronous generator G1 was 800 MW, and the fixed load $P_{L1} + jQ_{L1}$ was 1100 MW + 110 Mvar. AC area #2 contained two synchronous generators, namely G2 and G3 with the same capacity of 800 MW, and a constant power load $P_{L2} + jQ_{L2}$ of 2200 MW + 220 Mvar. All the generators were conventional synchronous machines represented using the sub-transient model and equipped with both a governor control (steam turbine) and an excitation system (IEEE-DC1A type) [27].

Recently, a coordinated droop strategy without communication was proposed for MTDC system in [23], [24]. We employed this droop controller for the GSVSC station, as described below.

A. GSVSC STATION DROOP CONTROLLER
The GSVSC station was equipped with a modified $P - V_{dc}$ droop controller considering the AC area frequency, as illustrated in Fig. 2.

The GSVSC controller was designed in the dq-axis. The active power and DC voltage can be controlled by tuning the d-axis current, while the reactive power and AC voltage can be controlled by tuning the q-axis currents. GSVSC1 and GSVSC2 were mainly responsible for regulating the DC voltage and transferring the injection power of the wind farms to the AC areas.
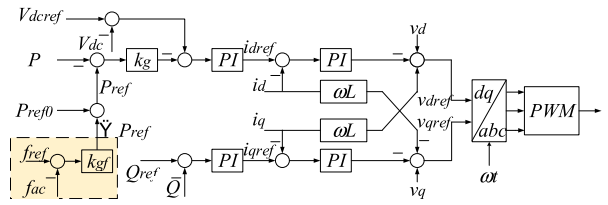

FIGURE 2. Block diagram of a typical controller for GSVSC.
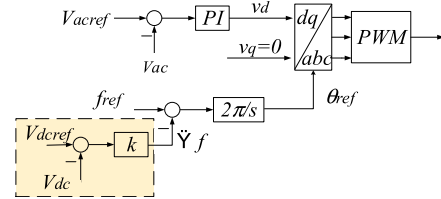

FIGURE 3. Typical VF control of the wind farm-side converter station.

From Fig. 2, it can be seen that when the system operates steadily, the relationship between V_{dc} and P is given by (1),

$$V_{dci} = V_{dcrefi} + k_{gi}\left(P_{refi} - P_i\right) \qquad (1)$$

where the subscript i represents the number of GSVSC stations, U_{dcrefi} is the normal DC-bus voltage, P_{refi} is the reference power with U_{dcrefi}, P_i is the measurement power of the GSVSC-i, and k_{gi} is the power droop coefficient of GSVSC-i that for provides the frequency support. P_{refi} is adjusted on the basis of the AC area frequency deviation and is expressed as follows,

$$P_{refi} = \Delta P_{refi} + P_{refi0} \qquad (2)$$

$$\Delta P_{refi} = k_{gfi}\left(f_{refi} - f_{aci}\right) \qquad (3)$$

where P_{refi0} is the initial reference power with nominal frequency, ΔP_{refi} is the additional frequency regulation reference power, k_{gfi} is the frequency droop coefficient, and f_{refi} is the nominal frequency.

When the AC area undergoes a frequency drop, a positive power increment ΔP_{refi} is calculated using (3) and added to the initial active power reference P_{refi0}. Thus, the injected active power for the AC areas increases through the grid-side station, thereby regulating the frequency of the AC areas.

Notably, based on the droop controller expressed in (1) and (3), an increase in the active power decreases the DC voltage. The reduced DC voltage influences the active power distributed among the GSVSC stations.

B. WIND FARM-SIDE VSC CONTROLLER
The wind farm-side VSC (WFVSC) stations, namely WFVSC1 and WFVSC2, were generally operated in the VF control mode, as shown in Fig. 3, to transmit the power of the wind farm.

For wind farm participation in the frequency regulation of the AC areas, a $V_{dc} - f$ droop control is added, as shown in the dashed box in Fig. 3. The wind farm frequency f_w^* is set using (4),

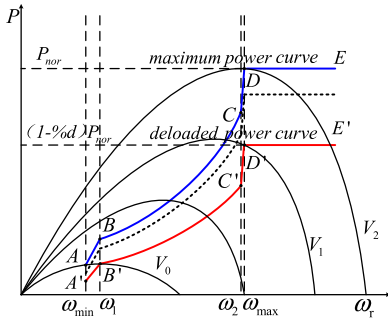$$f_{wi}^* = f_{ref} - k_i\left(V_{dcrefi} - V_{dci}\right) \qquad (4)$$

FIGURE 4. Maximum power curve and deloaded power curve for DFIG.

where f_{wi}^* is the set frequency of WFVSC-i, k_i is the voltage droop coefficient of WFVSC-i, and V_{dcrefi} and V_{dci} are the nominal and measurement values of the DC voltage of WFVSC-i, respectively.

By using (4), and taking the DC voltage as an intermediate variable, we can transmit the AC area frequency information to the wind farm.

C. DELOADED WIND FARM CONTROLLER
For the maximum power point tracking (MPPT) mode, the optimum power versus wind turbine rotor speed is commonly represented by equation (5), and see the black solid line in Fig. 4 [28].

$$P_{max} = \begin{cases} \dfrac{k_{opt}\omega_1^3}{\omega_1 - \omega_{min}}(\omega_r - \omega_{min}) & \omega_{min} \le \omega_r < \omega_1 \\ k_{opt}\omega_r^3 & \omega_1 \le \omega_r < \omega_2 \\ \dfrac{P_{nor} - k_{opt}\omega_2^3}{(\omega_{max} - \omega_2)} \\ \quad \times (\omega_r - \omega_{max}) + P_{nor} & \omega_2 \le \omega_r < \omega_{max} \\ P_{nor} & \omega_{max} \le \omega_r \end{cases} \quad (5)$$

where k_{opt} is optimization constant according to wind turbine aerodynamic characteristics.

With respect to Fig. 4, the segment AB (from ω_{min} to ω_1) is called the starting zone. And the segment BC (from ω_1 to ω_2) is the optimization zone, where is main operation zone for wind turbine. And the segment CD (from ω_2 to $\omega_{max}\omega_{max}$) is called constant rotor speed zone.

A deloaded power versus wind rotor speed is similarly defined by equation (6), which is illustrated by the red solid line in Fig. 2. The deloaded percentage is set 0.9 in this paper. And the deloaded control method diagram shows in Fig. 5.

$$P_{de} = \begin{cases} \dfrac{k_{de}\omega_1^3}{\omega_1 - \omega_{min}}(\omega_r - \omega_{min}) & \omega_{min} \le \omega_r < \omega_1 \\ k_{de}\omega_r^3 & \omega_1 \le \omega_r < \omega_2 \\ \dfrac{0.9P_{nor} - k_{de}\omega_2^3}{(\omega_{max} - \omega_2)} \\ \quad \times (\omega_r - \omega_{max}) + 0.9P_{nor} & \omega_2 \le \omega_r < \omega_{max} \\ 0.9P_{nor} & \omega_{max} \le \omega_r \end{cases}$$
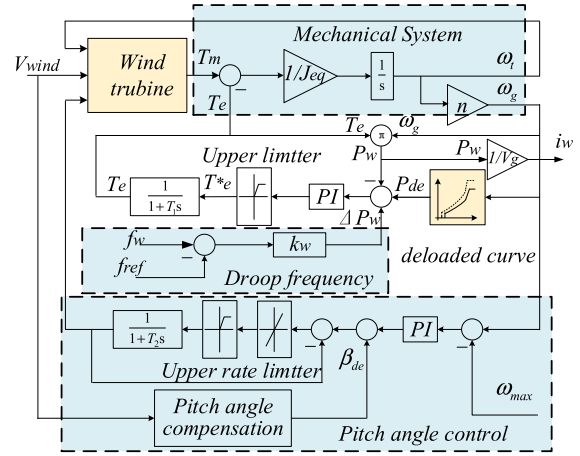
$$(6)$$

FIGURE 5. Simplified electromechanical model of DFIG-WT.

where k_{de} is deloaded constant according to wind turbine aerodynamic characteristics.

The deloaded power can be obtained depended on the deloaded power curve. However, in the medium and high wind speed conditions, because of the rotor speed limit, only using rotor speed control cannot realize a certain deloaded percentage [29]. A pitch angle control is necessary to help deloaded control for avoiding rotor speed over limit.

The pitch angle compensation method in [29] is used in the paper, as seen in Fig. 5. In [29], the deloaded control is divided into three areas, low wind speed area, medium wind speed area and high wind speed area according to the wind speed. And in the low wind speed area, only rotor speed control is used to realize deloaded control for wind turbine. And in the medium wind speed area and high wind speed area, additional pitch angle compensation is added to help realize deloaded control.

Based on the description in Section II, given that V_{dc}-f droop control is used for the WFVSC station, the frequency is determined by the WFVSC station, and it deviates from the nominal value if the DC voltage deviates.

An auxiliary frequency controller is used to generate an additional power, ΔP_w, which is added to the deloaded power, to provide frequency support,

$$\begin{aligned} P_{wref} &= P_{de} + \Delta P_w \\ &= P_{de} + k_w(f_{ref} - f_w) \end{aligned} \quad (7)$$

where P_{ref} is the reference active power, P_{de} is the deloaded active power; k_w is the droop coefficient of the auxiliary frequency controller, f_w is the measurement frequency of the WFVSC station; f_{ref} is the nominal frequency.

The wind farm can regulate the output power, utilizing the rotor kinetic energy from the wind turbine or the reserve power from the deloaded wind farms, to provide frequency support for the AC areas by sending additional power to the MTDC grid.

However, this coordinated droop control strategy inevitably leads to a DC voltage deviation when transmitting

the AC area frequency information. The allowable deviation in the DC voltage is limited, typically 10% of the normal value. The deviation in the DC voltage deteriorates the stability of the MTDC system. Reducing this deviation will enhance the stability and security of the MTDC system operation.

When wind farms participate in the frequency droop control, there still a part of the available energy is left for the deloaded wind farms. The reason is that if the frequency deviation does not reach the upper limit, the wind turbine does not work in the maximum power point tracking (MPPT) mode. Even if the frequency deviation reaches the upper limit, the wind turbine still has some available rotor kinetic energy.

In this study, we focused on virtual capacitor control for WFVSC stations. Unlike existing virtual inertia control methods, where the energy is derived from a DC capacitor, we utilized the rest energy of the deloaded wind farm to construct an AVC, without having to increase the capacity of the DC capacitor.

III. VIRTUAL INERTIA ANALYSIS OF DC POWER GRID
A. PRINCIPLE OF THE VIRTUAL CAPACITOR
In an AC system, the inertia reflects the ability of the system to prevent sudden changes in frequency. Generally, the so-called inertia constant H_s, defined as the ratio of the stored kinetic energy to the rated power of the plant, is used in AC systems to compare the inertial effect of generators with different ratings.

$$H_s = \frac{E_k}{S_n} = \frac{1}{2}\frac{J\omega^2}{S_n} \quad (8)$$

where E_k is the kinetic energy stored in the rotor at the rated speed; J is the generator inertia; ω is the mechanical speed; S_n is the rated capacity of the generator.

Similarly, for DC systems, the inertia constant H_{dc} can be defined as,

$$H_{dc} = \frac{W_k}{S_{vsc}} = \frac{1}{2}\frac{CV^2}{S_{vsc}} \quad (9)$$

where C is the capacitance of the parallel capacitor; W_{ki} is the electrical energy stored in C; S_{vsc} is the rated power capacity of the VSC station.

For the parameters listed in Table 1 (see in Section IV), $H_{dc} \approx 0.2$ s. Compared with synchronous generators of the same capacity, the inertia response is very low and is therefore neglected. Increasing the capacitance of the DC capacitor can increase the inertia constant for the DC system. Obviously, it increases the cost.

The dynamic electrical characteristic equation of the DC capacitor can be expressed as,

$$C_{dc}V_{dc}\frac{dV_{dc}}{dt} = P_{in} - P_{out} = \Delta P_{dc} \quad (10)$$

where P_{in} and P_{out} represent the input and output of the VSC station, respectively, and ΔP_{dc} is the mismatch power for the DC system.

Fortunately, owing to the fast and flexible power control of the VSC station, the additional power of the converter can be quickly absorbed or released via the VSC station control. Therefore, an additional power ΔP_{vsc} with respect to the rate of change in the DC voltage can be achieved via VSC active power control,

$$\Delta P_{VSC} = \frac{C_{vir}V_{dc}}{S_{VSC}} \cdot \frac{dV_{dc}}{dt} \quad (11)$$

With the incorporation of the additional power, ΔP_{vsc}, the dynamic characteristic equation of the DC capacitor can be modified as follows,

$$P_{in(p.u)} - P_{out(p.u)} = \Delta P_C + \Delta P_{VSC}$$
$$= C_{dc}V_{dc}\frac{dV_{dc}}{dt} + C_{vir}V_{dc}\frac{dV_{dc}}{dt} \quad (12)$$

According to (10), the additional power ΔP_{VSC}, obtained via the VSC station power control, can generate a virtual capacitor, C_{vir}. This provides more inertial support for the DC voltage. In this study, the additional power comes from the rest power of the deloaded wind farm.

B. VIRTUAL CAPACITOR CONTROL OF THE DELOADED WIND FARM
Fig. 6 shows the fixed virtual capacitor control of the WFVSC.
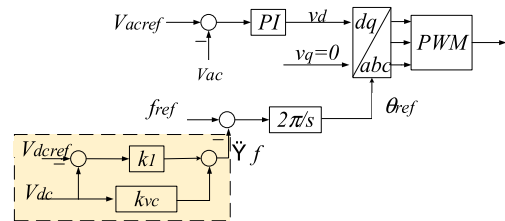
FIGURE 6. Simple inertial control of an inverter in a wind farm.

By improving the droop coefficient in (4), we propose a new droop characteristic for the WFVSC,

$$f_w = f_{wref} + \boldsymbol{k_{vc}}V_{dc} + k_1\left(V_{dc} - V_{dcref}\right) \quad (13)$$
$$\boldsymbol{k_{vc}} = k_2\frac{dV_{dc}}{dt} \quad (14)$$

where $\boldsymbol{k_{vc}}$ is a linear function of dV_{dc}/dt, and k_2 is the parameter of $\boldsymbol{k_{vc}}$.

When the DC voltage remains constant, dV_{dc}/dt is zero. The droop coefficient k_1 is the same as that in the conventional droop coefficient in (4). Once the DC voltage changes, dV_{dc}/dt will increase (or decrease). It increases k_2 and decreases dV_{dc}/dt. Therefore, the set frequency of the WFVSC station, f_w, increases (or decreases) compared to the one in the conventional droop control. Further, from (7), the wind farm injects more (or less) active power to the DC grids.

Comparing (4) with (13), we can rewrite f_w as,

$$f_w = f_w^* + k_2 V_{dc}\frac{dV_{dc}}{dt} \quad (15)$$

where f_w^* is the set frequency reference in (4).

With all the power losses neglected, the output power of the wind farm P_{wref} is equal to the injection power of the DC system, P_{in},

$$P_{in} = P_{wref} = P_{de} - k_w \cdot (f_w - f_{wref}) \tag{16}$$

Substituting (15) into (16) yields,

$$P_{in} = P_{in}^* - k_2 V_{dc} \frac{dV_{dc}}{dt} \tag{17}$$

where,

$$P_{in}^* = P_{de} - k_w \cdot (f_w^* - f_{ref}) \tag{18}$$

Substituting (17) into (10) yields,

$$CV_{dc}\frac{dV_{dc}}{dt} + k_w k_2 V_{dc}\frac{dV_{dc}}{dt} = P_{out} - P_{in}^* \tag{19}$$

From (19), the capacitance of the virtual capacitor C_{vir} can be determined as

$$C_{vir} = k_w k_2 \tag{20}$$

Therefore, through the modified droop control (expressed in (13)) for the WFVSC, compared with the conventional droop control, additional active power from the deloaded wind farm is injected to the DC grid. This provides an inertia support similar with a virtual capacitor. Evidently, it enhances the inertia of the dc bus. Further, the additional power eventually flows into the AC areas and improves the nadir of the frequency therein.

C. ADAPTIVE VIRTUAL CAPACITOR CONTROL

In (20), k_w is typically selected depending on the primary frequency response of the wind farms,

$$k_w = \frac{d\%P_{opt}}{\Delta f_{max}} \tag{21}$$

When k_w is fixed, the capacitance of the virtual capacitor is only determined by k_2. The higher the k_2 value, the higher the virtual capacitance C_{vir}. However, selecting k_2 is a difficult task because it depends on the operating state of the deloaded wind farm. If k_2 is set too large, the wind farm will excessively release energy, which may cause a DC voltage and frequency drop, thus failing to restore the rotor speed of the wind turbine. If k_2 is set too small, the reserve energy of the wind turbine will be underutilized.

An adaptive virtual control method is proposed in this section to address these issues. Utilizing the *arctan* function, i.e., an S-shaped curve, the nonlinear and adaptive k_{vc} is redefined,

$$k_{vc} = \begin{cases} \dfrac{K_{max}}{0.5\pi} arctan\left(k_a \dfrac{dV_{dc}}{dt}\right) & \dfrac{dV_{dc}}{dt} \geq 0 \\ \dfrac{-K_{min}}{0.5\pi} arctan\left(k_a \dfrac{dV_{dc}}{dt}\right) & \dfrac{dV_{dc}}{dt} < 0 \end{cases} \tag{22}$$

where K_{max} represents the maximum value of the virtual inertia droop coefficient, and K_{min} represents the minimum value.

Fig. 7 shows the curve of k_{vc} based on (22).

The curve of k_{vc} is S-shaped and can be divided into two sections: a saturation section and a linear section.
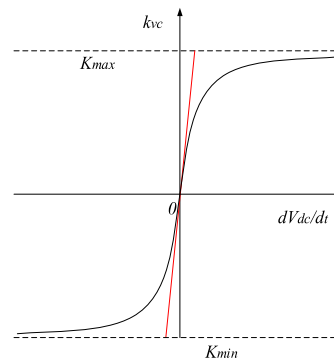
FIGURE 7. Curve of adaptive inertia droop coefficient k_{vc}.

D. LINEAR SECTION

When dV_{dc}/dt is low, the k_{vc} curve is approximately linear and can be approximated to a slope line as indicated by the red line in Fig. 7.

In the linear region, from (20), the slope of this line represents C_{vir}/k_w. From (22), the virtual capacitance, C_{vir}, is derived as follows,

$$C_{vir} = k_w k_{vc}' \big|_{\frac{dV_{dc}}{dt}=0} = \begin{cases} k_w \dfrac{K_{max}k_a}{0.5\pi}\dfrac{du}{dt} & \geq 0 \\ k_w \dfrac{-K_{min}k_a}{0.5\pi}\dfrac{du}{dt} & < 0 \end{cases} \tag{23}$$

Therefore, when the absolute value of dV_{dc}/dt is low, C_{vir} is redefined as in (23). This means that k_{vc} can be set a large value when dV_{dc}/dt is low, for providing better inertia support for the DC system.

E. SATURATION SECTION

When the absolute value of dV_{dc}/dt is high, the slope of k_{vc} is small. The value of k is infinitely close to K_{max} (or K_{min}) and never exceeds the limit, thus preventing the output power of the wind turbine from exceeding the maximum capacity and destabilizing the system.

Therefore, the S-shaped curve has two advantages: (i) It enables selecting a high k_{vc} value when dV_{dc}/dt is low, which helps provide better DC voltage support; (ii) It ensures that k_{vc} never exceeds the safe operation range when dV_{dc}/dt is high.

From (23), the capacitance of the virtual capacitor can be varied by adjusting the droop coefficient k_{vc}. Moreover, it is influenced by K_{max} and K_{min}. It is necessary to determine the maximum range of the droop curve under different conditions, i.e., K_{max} and K_{min}, to fully and reasonably use the rest energy of the deloaded wind farm on the basis of the above inertial control strategy.

The limit of the frequency deviation for the WFVSC station and the allowable range of the DC-bus voltage are as follows,

$$|\Delta f_w| < \Delta f_{wmax} = 0.2(24) \tag{24}$$

$$|\Delta V_{dc}| < \Delta V_{dcmax} = 0.1(p.u) \tag{25}$$

From (13), it can be observed that the GSVSC station controller provides both droop and inertia support by adjusting the set frequency deviation. k_1 represents the droop response and $\boldsymbol{k_{vc}}$ represents the inertia response, respectively. Evidently, $\boldsymbol{k_{vc}}$ will vary the set frequency deviation for the WFVSC station.

$$k_{vc} = \frac{(f_w - f_{wref}) - k_1(V_{dc} - V_{dcref})}{V_{dc}} \quad (26)$$

The values of K_{max} and K_{min} are defined via two scenarios: $V_{dc} \leq V_{dcref}$ and $V_{dc} > V_{dcref}$.

1. $V_{dc} \leq V_{dcref}$

When $V_{dc} < V_{dcref}$, it should avoid frequency deviation over the lower limit, $-\Delta f_{wmax}$. Thus, we have

$$k_{vc} \geq K_{min} = \frac{-\Delta f_{wmax} - k_1(V_{dc} - V_{dcref})}{V_{dc}} \quad (27)$$

If $\boldsymbol{k_{vc}}$ is lower than K_{min}, the frequency deviation exceeds the limit, which jeopardizes the safe operation of the wind farm system.

Similarly, to maintain the DC voltage in the safe-operation range, we use the following equation.

$$k_{vc} \leq K_{max} = \frac{(f_w - f_{wref}) + k_1 \Delta V_{dcmax}}{V_{dc}} \quad (28)$$

In (28), when $\boldsymbol{k_{vc}} = K_{max}$, the DC voltage deviation reaches the limit. Because the frequency is still f_w, if $\boldsymbol{k_{vc}} > K_{max}$, the DC bus will exceed the limit to obtain f_w, which hampers the stable operation of the frequency droop controller.

2. $V_{dc} > V_{dcref}$

The definitions of K_{max} and K_{min} are opposite in the case of $V_{dc} > V_{dcref}$.

When $V_{dc} > V_{dcref}$, it should avoid frequency deviation over the upper limit, Δf_{wmax}. Thus,

$$k_{vc} \leq K_{max} = \frac{\Delta f_{wmax} - k_1(V_{dc} - V_{dcref})}{V_{dc}} \quad (29)$$

Similarly,

$$k_{vc} \geq K_{min} = \frac{(f_w - f_{wref}) - k_1 \Delta V_{dcmax}}{V_{dc}} \quad (30)$$

K_{max} and K_{min} vary with the operating point of the system. Moreover, the virtual capacitance, C_{vir}, varies because of the variation in K_{max} and K_{min}.

Fig. 8 shows the AVC control for the WFVSC.

IV. SIMULATION RESULTS

A detailed four-terminal MTDC system simulation model, as pre-described in Section II, was built using the PSCAD/EMTDC software to validate the effectiveness of the proposed adaptive virtual capacitor control strategy. Table 1 lists the main parameters of the VSC-MTDC system. Table 2 lists the control parameters. Table 3 lists the parameters of the transmission line.

The droop controller of the grid-side VSC station follows the strategy proposed in [22], [23].

FIGURE 8. Adaptive virtual capacitor control of an inverter in a wind farm.

TABLE 1. Parameters of the VSC-MTDC system.

Item	VSC1	VSC2	VSC3	VSC4
Rated DC voltage (kV)	500	500	500	500
Rated AC voltage (kV)	260	260	260	260
Rated active power (MW)	300	600	300	600
Rated reactive power (MW)	0	0	0	0
Rated frequency (Hz)	50	50	50	50
DC capacitor capacitance (mF)	0.25	0.25	0.25	0.25
Bridge arm inductance (mH)	0.075	0.04	0.075	0.04

TABLE 2. Control parameters of the system.

Item	Value	Item	Value
k_{g1}	0.5	k_{gf1}	1
k_{g2}	0.25	k_{gf2}	1
k_1	2	k_a	200
k_2	5	k_w	30

TABLE 3. Parameters of the transmission line.

Item	Value
Line resistance (Ω/km)	0.0398
Line capacitance (μF/km)	0.0187
Line reactance (mH/km)	0.3956
Current limiting reactance (mH)	200
Line length of L1 (km)	149.1
Line length of L2 (km)	33
Line length of L3 (km)	75.3
Line length of L4 (km)	63

And three different strategies for the wind farm-side VSC station are simulated to demonstrate the advantages of the proposed AVC strategy:

1) No virtual capacitor control strategy (NVC).
2) Fixed virtual capacitor (FVC) control strategy
3) AVC control strategy;

A typical wind speed 10m/s is set in the paper, which stays in the medium wind speed area. Three scenarios are discussed below: a sudden load increase, a sudden load decrease and a sudden load increase with exchanging the synchronous generator capacity area #1 and area #2.
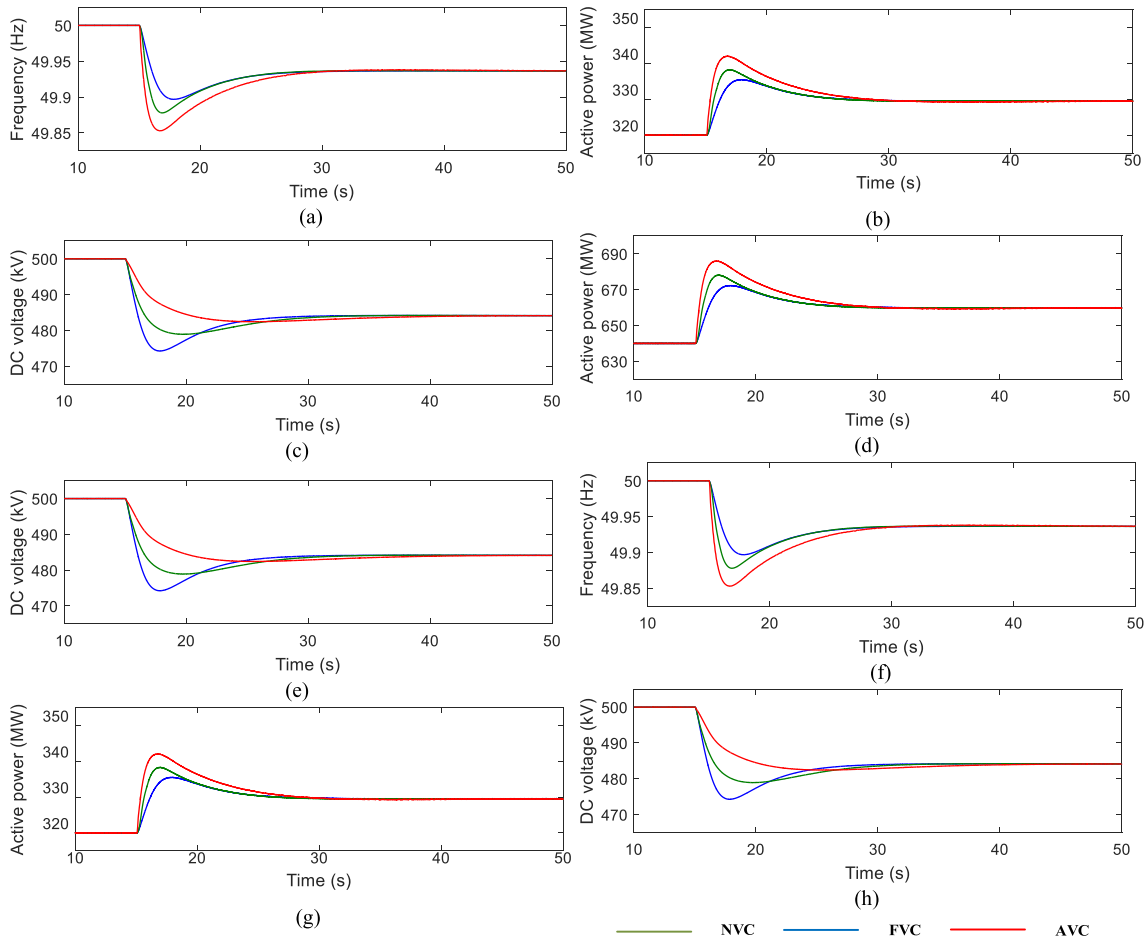
FIGURE 9. Simulation results for WFVSC side. (a) Frequency of WF1. (b) Rotor speed of WF1. (c) Pitch angle of WF1.
(d) Transmission power of WFVSC1. (e) DC voltage of WFVSC1. (f) Frequency of WF2. (g) Transmission power of WFVSC2.
(h) DC voltage of WFVSC2.

A. SCENARIO 1: SUDDEN INCREASE IN LOAD

The load of AC area #1 increases by 110 MW at t = 15 s, which causes an under-frequency event in AC area #1. The three different strategies, namely NVC, FVC, and AVC, are compared in Figs. 9, 10 and 11.

Fig. 9 shows the simulation curves for the wind farm side. The three control strategies reduce the DC voltage in both WF1 and WF2. The frequency for both the wind farms decreases, because of the coordinated droop controllers of the MTDC system. The wind farms increase the power injection to provide frequency support. The FVC and AVC strategies provide additional inertial response, without affecting the steady-state operation of the MTDC system. Thus, the three strategies eventually converge to the same steady-state operation. The difference is in the transient process.

And Fig. 9 (b) and (c) shows the simulation curves of the rotor speed and pitch angle of WF1. Because wind speed 10m/s stays in medium speed area, both of the rotor speed and pitch angle are used to realize the deloaded control. And both of them decrease to increase the output active power from the deloaded wind turbine.

In the NVC strategy, the DC voltage nadir is higher, the frequency drop is the lowest, and the increase in the injection power from the two wind farms is the least. This is because the frequency of the WFVSC is only influenced by the DC voltage deviation instead of both dV_{dc}/dt and DC voltage deviation as observed in the FVC and AVC strategies.

In the FVC strategy, because of the additional inertial power provided, although the DC voltage dip is greater than that in the NVC strategy, the decrease in the frequency and the increase in the power from the wind farm are greater.

In the AVC strategy, although the nadir of V_{dc} is the lowest, the decrease in the frequency of the WFVSC is most significant, and the output power for the wind farm is the highest. Because the virtual capacitor can adaptively adjust the operating state of the system, it can provide more inertial power from the wind farm. Fig. 10 shows the k_{vc} values of the three strategies.

As shown in Fig. 10, k_{vc} in the NVC strategy is zero, which means that this strategy cannot provide an inertial response. In the FVC and AVC strategies, k_{vc} varies with the rate of DC voltage change.
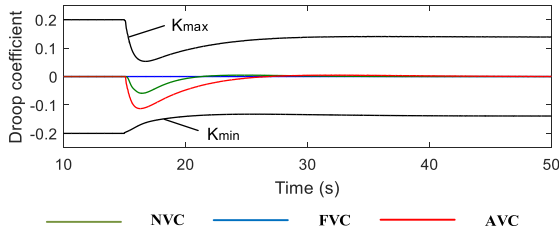
FIGURE 10. Simulation results of k_{vc}.

For NVC strategy, the deloaded wind farm does not participate into the inertial response, and the additional inertia time constant from deloaded wind farms is zero obviously; for FVC strategy, according to formula (9) and the parameters in Table 2, The inertia constant time from the virtual capacitor is 1.64s; for AVC strategy, the inertia time constant from deloaded wind farms is a variable value because of the variation of the value of the virtual capacitor. At the initial time of the frequency event, the additional inertia constant time is 6.54s; and in the end it drops to 4.12s. Obviously, AVC strategy provides the best inertia response from the deloaded wind farm among the three control strategies.

The values of K_{max} and K_{min} indicate the range of k_{vc}. K_{max} increases with the increase in the frequency of the WFVSC. K_{min} is a negative value and increases with the decrease in the DC voltage. K_{max} and K_{min} vary with the system operating state. k_{vc} for AVC strategy varies with the change in K_{max} and K_{min}. The value of k_{vc} for AVC strategy is selected such that its value is higher than the FVC strategy, for better utilizing the available power from the deloaded wind farm.

Notably, dV_{dc}/dt is rather small when the Vdc voltage is recovered ($dV_{dc}/dt > 0$). Consequently, the value of k_{vc} is also a very small value. Thus, if the load suddenly increases, the influence of the variation in K_{max} is slight. The main factor is K_{min}.

Fig. 11 shows the simulation curves of the GSVSC stations. The increased load of AC area #1 leads to a frequency drop event in AC area #1. The frequency deviation in AC area #1 causes a DC bus voltage drop through the coordinated droop controller of the MTDC system. The power injected to AC area #1 increases, and the DC-bus voltage drops because of the frequency-power-DC voltage droop controller.

The DC-bus voltage drop leads to a decrease in the power injected to AC area #2. Subsequently, the frequency of AC area #2 decreases. This means that AC area #2 provides some frequency support for AC area #1 at the expense of the frequency drop in AC area #2.

For the three strategies, Tables IV and V list the frequency nadirs of the AC areas and DC voltage nadirs of the four terminals, respectively.

In the NVC strategy, although the DC voltage nadir and the frequency nadir are the highest, the power injected to AC area #1 is the lowest. This is because the NVC strategy does not provide a virtual inertia support from the deloaded wind farm. The reduction in the power injected to AC area #2 is the highest because the DC voltage drop is the highest.
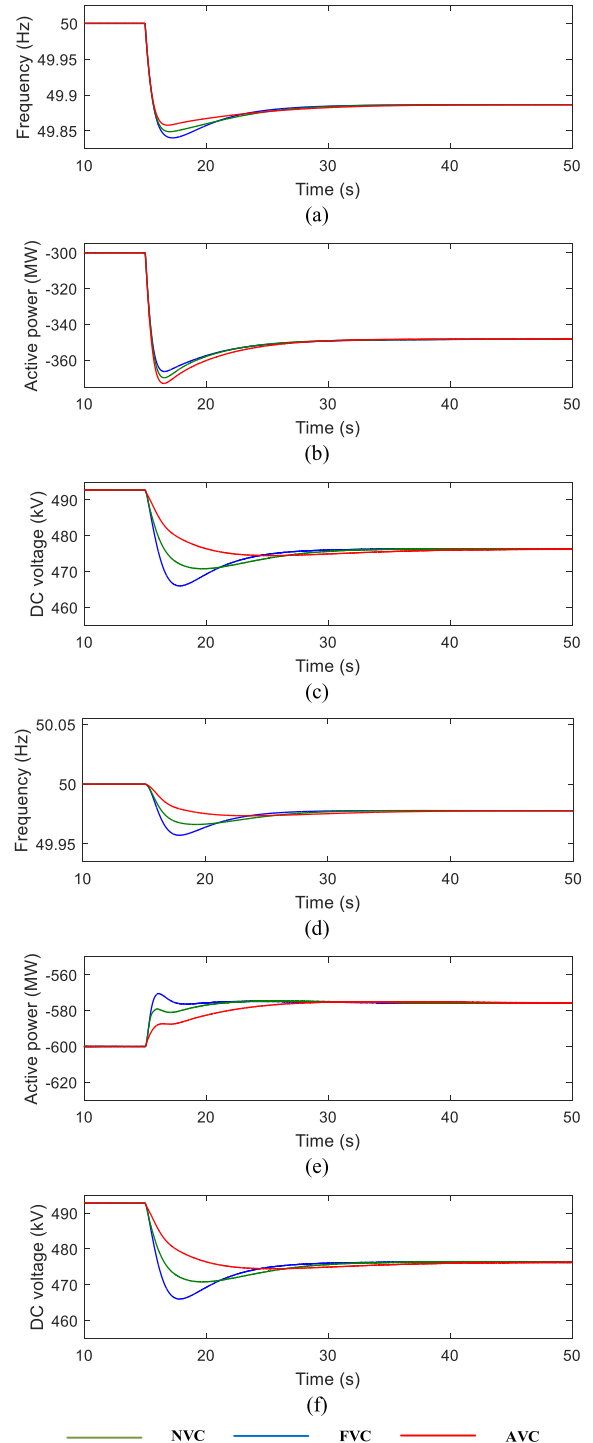

FIGURE 11. Simulation results of GSVSC side. (a) Frequency of AC area #1. (b) Transmission power of GSVSC1. (c) DC voltage of GSVSC1. (d) Frequency of AC area #2. (e) Transmission power of GSVSC2. (f) DC voltage of GSVSC2.

The frequency nadirs of AC area #1 and AC area #2 are the highest.

In the FVC strategy, because of the additional inertial power from the deloaded wind farm, the DC voltages of GVSC1 and GVSC2 are lower than those in the NVC strategy. The reduction in the power injected to AC area #2 is lower
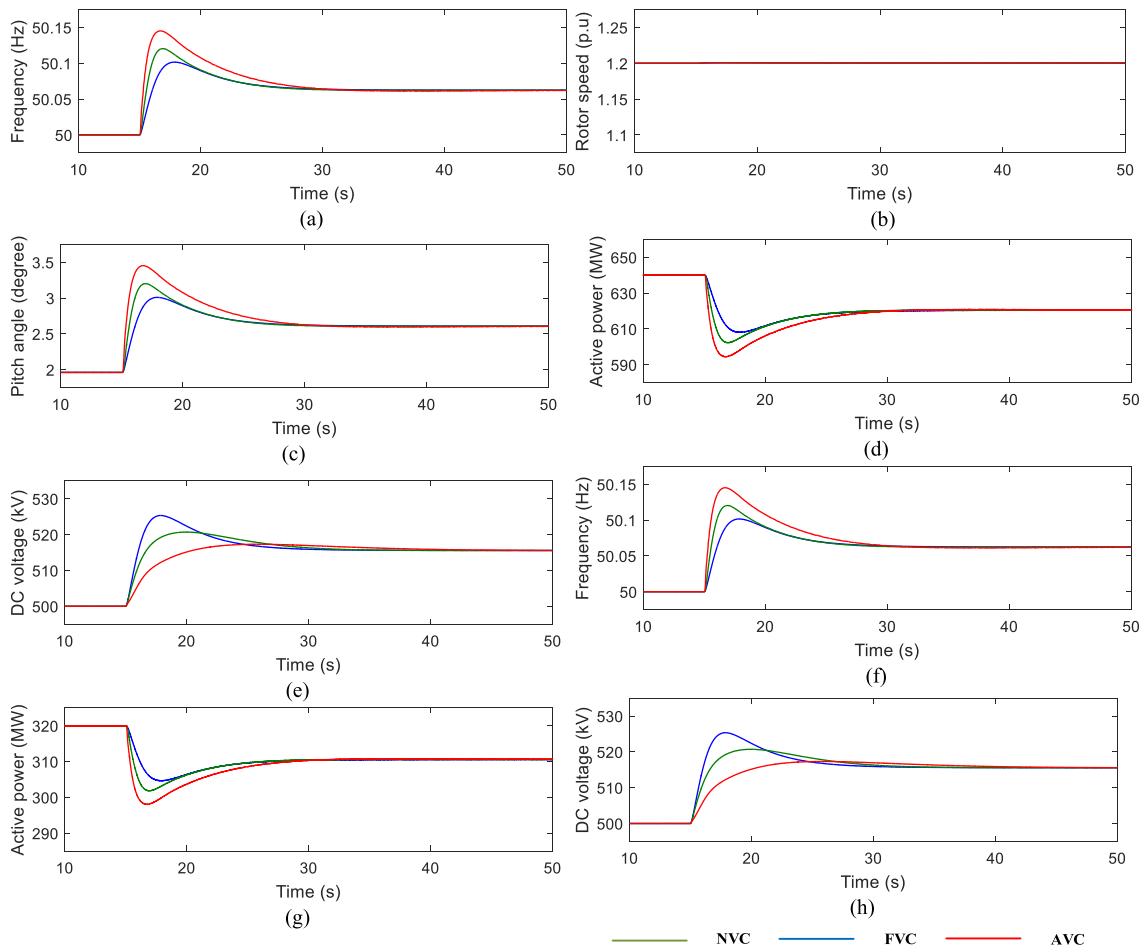
FIGURE 12. Simulation results for WFVSC side. (a) Frequency of Wf1. (b) Rotor speed of WF1. (c) Pitch angle of WF1. (d) Transmission power of WFVSC1. (e) DC voltage of WFVSC1. (f) Frequency of WF2. (g) Transmission power of WFVSC2. (h) DC voltage of WFVSC2.

TABLE 4. Comparision of the dc voltage nadir.

nadir of DC voltage/kV	WFVSC1	WFVSC2	GSVSC3	GSVSC4
NVC	474.26	474.26	466.02	466.40
FVC	478.92	478.92	470.82	471.20
AVC	482.45	482.45	474.42	474.80

TABLE 5. Comparision of the frequency nadir.

nadir of frequency/Hz	WF1	WF2	AC area #1	AC area #2
NVC	49.897	49.897	49.840	49.958
FVC	49.878	49.878	49.849	49.966
AVC	49.854	49.854	49.858	49.974

than that in the NVC strategy. The frequency nadirs of AC area #1 and AC area #2 are better than the ones in the NVC strategy.

In the AVC strategy, because of the additional inertial power from the deloaded wind farms, the nadir of V_{dc} is the lowest, and the frequency nadirs of AC area #1 and AC area #2 are the lowest. The reduction in the power injected to AC area #2 is the lowest.

Briefly, the proposed AVC strategy can adaptively adjust the value of its k_{vc} and provide more virtual inertia support for the DC voltage, thereby improving the nadir of the DC voltage. Furthermore, the additional power from the deloaded wind farms eventually flows into the AC area and improves the frequency nadir of the AC area.

B. SCENARIO 2: SUDDEN REDUCTION IN LOAD
The load of AC area #1 is reduced by 110 MW at t = 15 s, which causes an up-frequency event in AC area #1.

Fig. 12 illustrates the simulation curve for the wind farm side. The frequency rise in AC area #1 causes a DC voltage drop in both WF1 and WF2. As a result, the frequency for both the wind farms increases, and the injection power decreases. Comparing the three strategies, the NVC strategy yields the highest DC voltage peak, followed by the FVC strategy, and finally the AVC strategy. Because of the rotor speed has reached the maximum value, only the pitch angle increases to reduce the output active power from the wind farm.
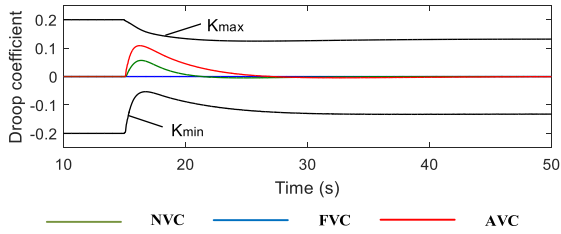
FIGURE 13. Simulation results of k_{vc}.

TABLE 6. Comparision of the dc voltage peak.

peak of DC voltage/kV	WFVSC1	WFVSC2	GSVSC3	GSVSC4
NVC	525.33	525.33	519.05	518.64
FVC	520.70	520.70	514.32	513.92
AVC	517.30	517.30	510.78	510.44

TABLE 7. Comparision of the frequency peak.

peak of frequency/Hz	WF1	WF2	AC area #1	AC area #2
NVC	50.100	50.100	50.159	50.042
FVC	50.120	50.120	50.150	50.033
AVC	50.145	50.145	50.142	50.026

Fig. 13 shows the k_{vc} values for the AVC and FVC strategies. k_{vc} for the NVC strategy is zero. K_{max} decreases with the increase in the DC voltage. K_{min} is a negative value and increases with the increase in the frequency of the WFVSC. k_{vc} for the AVC strategy is higher than that for the FVC strategy.

When the DC voltage is recovered ($dV_{dc}/dt < 0$), the dV_{dc}/dt and k_{vc} values are very low. The influence of the variation in K_{min} is minor.

Fig. 14 shows the simulation curve of the AC area. The frequency of AC area #1 increases because of the sudden decrease in the load, the power injected into AC area #1 decrease, and the DC-bus voltage increases because of the frequency-power-DC voltage droop controller.

Because of the increase in the DC voltage, the power injected to AC area #2 increases, and the frequency of AC area #1 increases. This implies that AC area #2 provides some frequency support for AC area #1 at the expense of increasing the frequency in AC area #2.

For the three strategies, Tables VI and VII list the peak frequency and DC voltage peak of the four-terminal system. The NVC strategy yields the highest DC voltage peak, followed by the FVC strategy, and finally the AVC strategy. The NVC strategy has the highest frequency peaks in AC area #1 and AC area #2, followed by the FVC strategy, and AVC strategy. Owing to the proposed AVC strategy, the DC voltage and frequency of the AC area are improved to a greater extent when compared with the other two strategies.
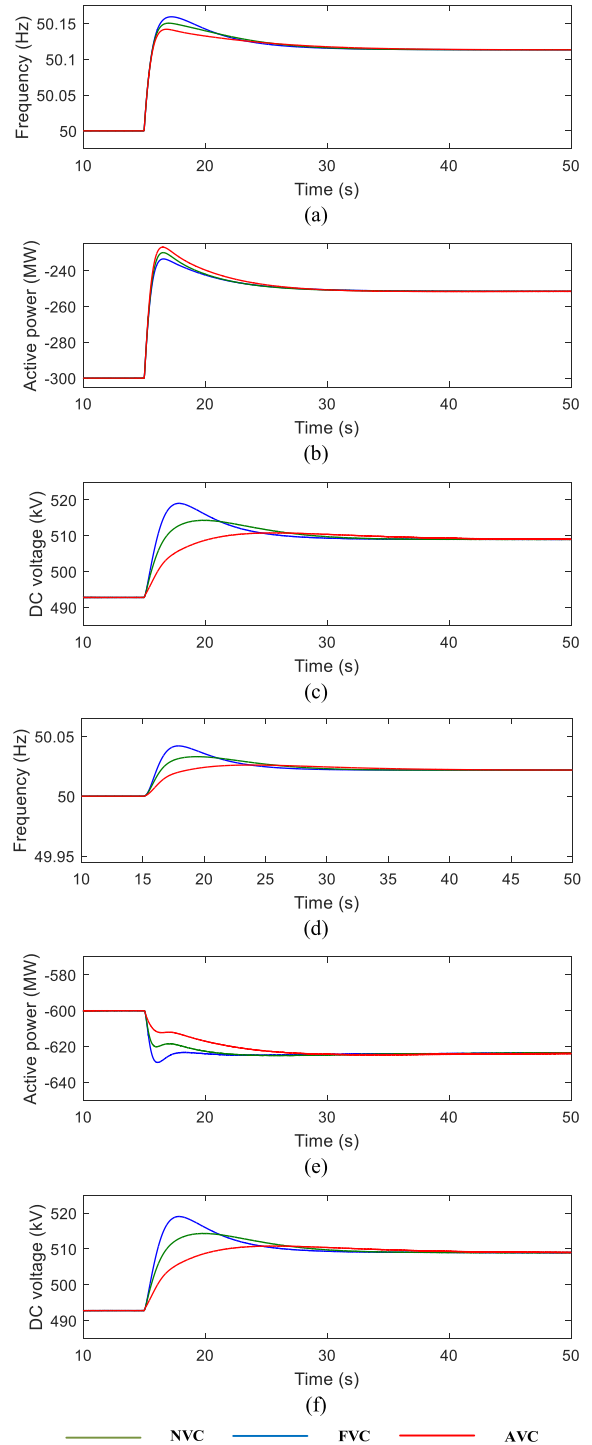

FIGURE 14. Simulation results of GSVSC side. (a) Frequency of AC area #1. (b) Transmission power of GSVSC1. (c) DC voltage of GSVSC1. (d) Frequency of AC area #2. (e) Transmission power of GSVSC2. (f) DC voltage of GSVSC2.

C. SCENARIO 3: EXCHANGING AC AREA #1 AND AC AREA #2

The positions of the AC area #1 and the AC area #2 are exchanged. That is, the synchronous generator capacity area #1 is 1600MVA, and the synchronous generator capacity area #2 is 800MVA. The load of AC area #1 increases
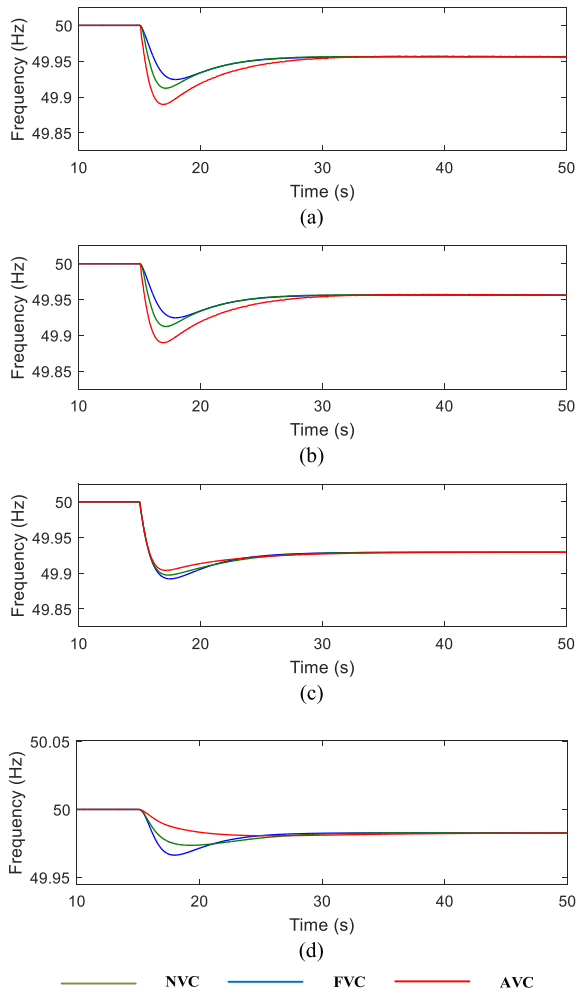
FIGURE 15. Simulation results for frequency (a) Frequency of Wf1. (b) Frequency of Wf2. (c) Frequency of AC area #1. (d) Frequency of AC area #1. (e) Transmission power of WFVSC2. (f) DC voltage of WFVSC2.

FIGURE 16. Simulation results of DC voltage. (a) DC voltage of WFVSC1. (b) DC voltage of WFVSC2. (c) DC voltage of GSVSC1. (d) DC voltage of GSVSC2.

TABLE 8. Comparision of the dc voltage nadir.

nadir of DC voltage/kV	WFVSC1	WFVSC2	GSVSC3	GSVSC4
NVC	481.14	481.14	473.22	473.46
FVC	484.85	484.85	477.02	477.22
AVC	486.64	486.64	478.90	478.66

TABLE 9. Comparision of the frequency nadir.

nadir of frequency/Hz	WF1	WF2	AC area #1	AC area #2
NVC	49.924	49.924	49.892	49.966
FVC	49.913	49.913	49.898	49.974
AVC	49.890	49.890	49.904	49.980

by 110 MW at t = 15s, which causes an under-frequency event in AC area #1.

Fig. 15 shows the frequency waveforms for the four AC systems, and Fig. 16 shows the DC voltage waveforms for the four terminal converter stations.

These simulation results are similar with the ones for scenario 1. The frequency drop event in AC area #1 causes a DC voltage drop. Then DC voltage drop results to the two deloaded wind farm release more active power. And the active power injected into AC area #2 decreases and it causes a frequency drop in AC area#2.

The frequency nadir and DC voltage nadir of the four-terminal system are summarized in the Table 8 and IX. Compare with the results in Scenario 1, for all the three control strategies, the nadir of the four terminals DC voltage and the nadir of AC frequency in scenario 3 are higher than those in scenario 1. In our views, because synchronous generator capacity AC area #1 > synchronous generator capacity AC area #2, the same load change result a slighter frequency dip. And then, the DC voltage and AC frequency in other areas also show a slighter change.
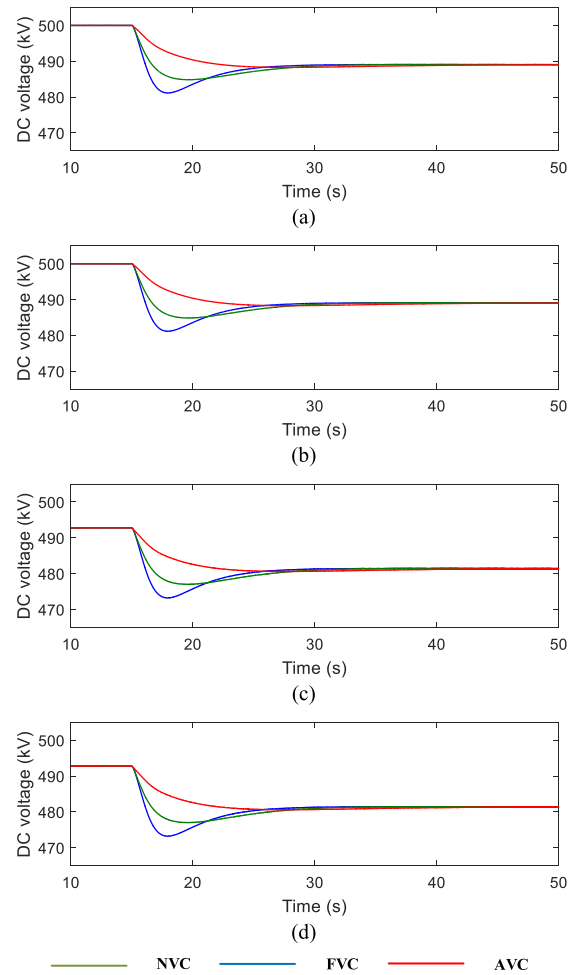
V. CONCLUSION

In this study, we developed an adaptive virtual capacitor control strategy for an MTDC system with deloaded wind farms. In this strategy, the rest energy of the deloaded wind farm was utilized to generate a virtual capacitor that can support DC voltage and AC area grid frequency. Furthermore,

an S-shape function was used to adaptively adjust the value of the virtual capacitor, which is limited by the MTDC system operating state, to provide a better inertial response than the fixed virtual capacitor control strategy.

A four-terminal VSC-based MTDC system comprising two wind farms model was built. The feasibility and advantages of the proposed virtual capacitor control strategy were demonstrated and validated using a detailed simulation model. The compared simulation results showed that the proposed strategy can effectively enhance the DC voltage and frequency nadirs of the AC system.

However, only the simulation results are provided for validating the effectiveness of the proposed strategy theoretically. In the future, we will try to build the MTDC experimental system and seek the cooperation opportunities with power grid companies and apply the strategy into the real industry application.

REFERENCES

[1] Global Wind Energy Council. (2019). *Global Wind Report*. [Online]. Available: https://gwec.net/global-wind-report-2019/

[2] G. Tang, Z. He, and H. Pang, "Discussion on applying the VSC-HVDC technology in global energy interconnection," *Smart Grid*, vol. 4, no. 2, pp. 116–123, Feb. 2016.

[3] S. S. H. Yazdi, J. Milimonfared, S. H. Fathi, and K. Rouzbehi, "A comprehensive VSG-based onshore FRT control strategy for OWFs with VSC-MT-HVDC transmission," *IEEE Access*, early access, Oct. 15, 2019, doi: 10.1109/ACCESS.2019.2945919.

[4] H. Pang and X. Wei, "Research on key technology and equipment for Zhangbei 500 kV DC grid," in *Proc. Int. Power Electron. Conf. (IPEC-Niigata-ECCE Asia)*, Niigata, Japan, May 2018, pp. 2343–2351, doi: 10.23919/IPEC.2018. 8507575.

[5] A. Sarlette, J. Dai, Y. Phulpin, and D. Ernst, "Cooperative frequency control with a multi-terminal high-voltage DC network," *Automatica*, vol. 48, no. 12, pp. 3128–3134, Dec. 2012.

[6] J. Dai, Y. Phulpin, A. Sarlette, and D. Ernst, "Coordinated primary frequency control among non-synchronous systems connected by a multi-terminal high-voltage direct current grid," *IET Gener., Transmiss. Distrib.*, vol. 6, no. 2, pp. 99–108, 2012.

[7] J. Zhu, C. D. Booth, G. P. Adam, A. J. Roscoe, and C. G. Bright, "Inertia emulation control strategy for VSC-HVDC transmission systems," *IEEE Trans. Power Syst.*, vol. 28, no. 2, pp. 1277–1287, May 2013.

[8] J. Zhu, C. D. Booth, W. Hung, J. M. Guerrero, and G. P. Adam, "Generic inertia emulation controller for multi-terminal voltage-source-converter high voltage direct current systems," *IET Renew. Power Gener.*, vol. 8, no. 7, pp. 740–748, Sep. 2014.

[9] M. Ashabani and Y. A.-R.-I. Mohamed, "Novel comprehensive control framework for incorporating VSCs to smart power grids using bidirectional synchronous-VSC," *IEEE Trans. Power Syst.*, vol. 29, no. 2, pp. 943–957, Mar. 2014.

[10] H. Liu and Z. Chen, "Contribution of VSC-HVDC to frequency regulation of power systems with offshore wind generation," *IEEE Trans. Energy Convers.*, vol. 30, no. 3, pp. 918–926, Sep. 2015.

[11] Y. Phulpin, "Communication-free inertia and frequency control for wind generators connected by an HVDC-link," *IEEE Trans. Power Syst.*, vol. 27, no. 2, pp. 1136–1137, May 2012.

[12] B. Silva, C. L. Moreira, L. Seca, Y. Phulpin, and J. A. P. Lopes, "Provision of inertial and primary frequency control services using offshore multi-terminal HVDC networks," *IEEE Trans. Sustain. Energy*, vol. 3, no. 4, pp. 800–808, Oct. 2012.

[13] M. Kayikci and J. V. Milanovic, "Dynamic contribution of DFIG-based wind plants to system frequency disturbances," *IEEE Trans. Power Syst.*, vol. 24, no. 2, pp. 859–867, May 2009.

[14] M. El Mokadem, V. Courtecuisse, C. Saudemont, B. Robyns, and J. Deuse, "Experimental study of variable speed wind generator contribution to primary frequency control," *Renew. Energy*, vol. 34, no. 3, pp. 833–844, Mar. 2009.

[15] L.-R. Chang-Chien, W.-T. Lin, and Y.-C. Yin, "Enhancing frequency response control by DFIGs in the high wind penetrated power systems," *IEEE Trans. Power Syst.*, vol. 26, no. 2, pp. 710–718, May 2011.

[16] E. Jahan, R. Md Hazan, S. M. Muyeen, A. Umemura, R. Takahashi, and J. Tamura, "Primary frequency regulation of the hybrid power system by deloaded PMSG-based offshore wind farm using centralised droop controller," *IET J. Eng.*, vol. 2019, no. 18, pp. 4590–4594, 2019.

[17] A. Junyent-Ferre, Y. Pipelzadeh, and T. C. Green, "Blending HVDC-link energy storage and offshore wind turbine inertia for fast frequency response," *IEEE Trans. Sustain. Energy*, vol. 6, no. 3, pp. 1059–1066, Jul. 2015.

[18] F. D. Bianchi and J. L. Dominguez-Garcia, "Coordinated frequency control using MT-HVDC grids with wind power plants," *IEEE Trans. Sustain. Energy*, vol. 7, no. 1, pp. 213–220, Jan. 2016.

[19] M. Andreasson, R. Wiget, D. V. Dimarogonas, K. H. Johansson, and G. Andersson, "Coordinated frequency control through MTDC transmission systems," *IFAC-PapersOnLine*, vol. 48, no. 22, pp. 106–111, 2015.

[20] M. Andreasson, R. Wiget, D. V. Dimarogonas, K. H. Johansson, and G. Andersson, "Distributed frequency control through MTDC transmission systems," *IEEE Trans. Power Syst.*, vol. 32, no. 1, pp. 250–260, Jan. 2017.

[21] A. Kirakosyan, E. F. El-Saadany, M. S. E. Moursi, and K. A. Hosani, "DC voltage regulation and frequency support in pilot voltage droop controlled multi terminal HVDC systems," *IEEE Trans. Power Del.*, vol. 33, no. 3, pp. 1153–1164, Jun. 2018.

[22] W. Wang, Y. Li, Y. Cao, U. Hager, and C. Rehtanz, "Adaptive droop control of VSC-MTDC system for frequency support and power sharing," *IEEE Trans. Power Syst.*, vol. 33, no. 2, pp. 1274–1564, Mar. 2018.

[23] N. R. Chaudhuri, R. Majumder, and B. Chaudhuri, "System frequency support through multi-terminal DC (VSC-MTDC) grids," *IEEE Trans. Power Syst.*, vol. 28, no. 1, pp. 347–356, Feb. 2013.

[24] T. M. Haileselassie and K. Uhlen, "Primary frequency control of remote grids connected by multi-terminal HVDC," in *Proc. IEEE PES Gen. Meeting*, Jul. 2010, pp. 1–6.

[25] A. Heidary, H. Radmanesh, K. Rouzbehi, and J. Pou, "A DC-reactor-based solid-state fault current limiter for HVdc applications," *IEEE Trans. Power Del.*, vol. 34, no. 2, pp. 720–728, Apr. 2019.

[26] A. Heidary, K. Rouzbehi, M. Hesami, M. Bigdeli, and C. Bordons, "Bridge-type fault current limiter and hybrid breaker for HVDC grids applications," *IET Gener., Transmiss. Distrib.*, vol. 14, no. 18, pp. 3913–3919, Sep. 2020.

[27] *IEEE Recommended Practice for Excitation System Models for Power System Stability Studies*, IEEE Standard 421.5-2005 (Revision of IEEE Std. 421.5-1992), Apr. 2006, pp. 1–85.

[28] D. Ochoa and S. Martinez, "Fast-frequency response provided by DFIG-wind turbines and its impact on the grid," *IEEE Trans. Power Syst.*, vol. 32, no. 5, pp. 4002–4011, Sep. 2017.

[29] P. Li, W. Hu, R. Hu, Q. Huang, J. Yao, and Z. Chen, "Strategy for wind power plant contribution to frequency control under variable wind speed," *Renew. Energy*, vol. 130, pp. 1226–1236, Jan. 2019, doi: 10.1016/j.renene.2017.12.046.

CHENG ZHONG (Member, IEEE) was born in Jiangxi, China, in 1985. He received the B.S. degree from the Harbin Institute of Technology, Harbin, China, in 2007, and the M.S. and Ph.D. degrees in power systems and automation from China Agricultural University, Beijing, China, in 2010 and 2014, respectively. He is currently an Assistant Professor with the School of Electrical and Electronic Engineering, Northeast Electric Power University, Jilin, China, where he has been since 2014. His current research interests include the area of power system distribute intelligent control, power system frequency regulation by renewable power.

JIALONG ZHANG (Graduate Student Member, IEEE) was born in Jilin, China, in 1995. He received the B.S. degree from Northeast Electric Power University, in 2018, where he is currently pursuing the M.E. degree in electrical engineering. His research interest includes frequency adjustment of multi-terminal flexible DC systems.

YANG ZHOU (Graduate Student Member, IEEE) was born in Qingdao, China, in 1996. He received the B.S. degree from Qufu Normal University, Rizhao, in 2018. He is currently pursuing the M.E. degree in electrical engineering from Northeast Electric Power University. His research interest includes power system frequency regulation by renewable power.

● ● ●